Physical models at increasing scale and role of theoretical / numerical back-analyses

Enrique Romero*-Guido Musso-Cristina Jommi*****

** Universitat Politècnica de Catalunya*
Department of Geotechnical Engineering and Geosciences
c/ Jordi Girona, 1-3, Campus Nord UPC, Building D-2
08034 Barcelona, Spain
enrique.romero-morales@upc.edu

***Politecnico di Torino*
Dipartimento di Ingegneria Strutturale, Edile e Geotecnica
Corso Duca degli Abruzzi, 24
10129 Torino, Italy

****Politecnico di Milano*
Dipartimento di Ingegneria Strutturale
piazza Leonardo da Vinci, 32
20133 Milano, Italy

In spite of advancements in the techniques for the study of thermo-hydro-chemo-mechanical behaviour of geomaterials at the REV scale, the latter might not provide an exhaustive picture of transport processes in soil, when non-linear coupling terms arise, and when scale effects are expected. To overcome the difficulties associated with this issue, physical models, in which relevant coupled fields may be tracked in time, can be developed. Most often, theoretical and / or numerical models must accompany the interpretation of the physical test, to exploit all the information provided by measurements. In this chapter a few examples of increasing complexity are briefly presented to discuss this viewpoint and to show the potentialities provided by physical models aided by theoretical and numerical interpretation in the comprehension of coupled behaviour.

1 Introduction

Geomechanics and geo-environmental engineering problems, such as earth constructions, waste confinement at surface or at great depths, soil pollution and remediation, often involve heat, mass and contaminant transport. These processes cannot be fully understood unless a clear picture of coupled thermo-hydro-chemo-mechanical behaviour of geomaterials is drawn. Despite advancements in experimental techniques developed to study these processes (refer to the previous chapters), and despite the development of refined control techniques, issues remain regarding the effects promoted by the coupling terms and their interpretation.

On the one hand, control conditions may be imposed only on the boundary of the specimen at the macroscopic, or phenomenological, scale. Homogeneity of the relevant fields inside the specimen is not guaranteed when transport processes occur. On the other hand, control may be applied only to direct fields, but indirect processes, arising as a consequence of primary gradients, evolve independently from any external control. Non-linearity, which almost always characterise the behaviour of soils under any coupled field, further complicate full understanding of the soil response.

As a consequence, detailed experimental information on the local distribution of the relevant field quantities usually remains unknown, unless local/tomographic experimental data are provided (see, for instance, the previous chapter on experimental techniques for multi-scale description of soil fabric). If not, theoretical back-analysis or numerical simulation aided techniques seem to be mandatory to interpret the experimental information and better define the soil response to external loading.

In this chapter a few examples, from previous physical models of the authors, are presented to contribute to this discussion. Firstly, experimental setup of cells at laboratory scale (bench/mock-up scale) equipped with different combinations of chemo-thermo-hydro-mechanical controlled conditions at the boundary are presented. The cells were developed and used in the study of a number of multi-physics processes in geomaterials, within the context of different investigations:

- soil-atmosphere interaction for the prediction of local water balance in upper unsaturated soils [Car11a, b];
- thermal loads effects on saturated geomaterials in the performance of low-permeability argillaceous formations proposed as potential radioactive waste repository [Muñ09, Lim10, Lim11];
- air migration and air pressure breakthrough processes in low permeability argillaceous formations and their role in the onset of air pathways [Rom10, Rom12a,b];
- electrical resistivity tomography in the study of salt transport, wetting processes and water retention properties at the bench scale [Com11, Cos12].

The examples are accompanied by comments on the use of theoretical back-analysis and numerical simulation tools for the understanding of the evolutionary processes at the local scale. Theoretical and numerical models are useful to evidence which, among several possible coupled / multiscale phenomena, have a significant role on

the investigation of concern. Then they provide complementary information on the evolution of local variables, due to coupled interaction mechanisms, and also offer a possible interpretation tool for checking reliability of experimental results.

In the numerical modelling of all these coupled problems a huge amount of information on the material behaviour is usually needed. Given also simple models, a large number of material parameters are usually involved, which, in some cases, can be evaluated directly from purportedly designed laboratory tests. However, in most cases, when coupled processes are involved, back-analysis of laboratory experiments specifically designed to highlight the relevant processes associated with the unknown parameters are necessary. Carrying out a back-analysis of the boundary value test allows better identification of some model parameters which cannot be easily derived from direct experimental information on a homogeneous REV, by means of the definition and the minimisation of an objective function, which depends on the differences between measured and computed variables. The suggested procedure is not free of drawbacks, it may admit more than one solution, and a certain degree of judgment must be always put in interpreting the data, as the following examples help in showing.

2 Hydraulic boundary value model column for soil-atmosphere interaction

2.1 Introduction

Water balance resulting from the transport processes taking place in the unsaturated zone is a key factor in the hydrological and mechanical processes responsible for slope instability and shallow landslides. Infiltration and evaporation affect shallow water-table fluctuations, groundwater recharge, and groundwater contamination. Spatial and temporal distribution of rain and evaporation are the forcing climatic conditions at the boundary of the soil system. Infiltration and evaporation hydrologic models, based on climatic forcing conditions only, are most often adopted to predict the water balance in the subsoil, while scarce information on the soil water retention and transport properties are introduced in these models. This approach has two obvious drawbacks. Firstly the soil properties contribute to determine infiltration and evaporation capacity of the soil in a different way as a function of the seasonal conditions. Secondly, these purely hydrologic models can reproduce quite well the water content evolution in the upper soil layers, if properly trained on some historical data, but they will lose their predictive capabilities, when changes should intervene in the climatic conditions or in the soil properties.

To overcome these drawbacks, and provide predictive tools which could account for changing scenarios, numerical models can be developed. Accurate description of the actual physical processes requires the solution of a non-isothermal problem account-

ing for two-phase liquid and vapour transport (e.g. [Phi57, Mil84]). When models of the latter class are designed, concerns may arise on the best way to translate meteorological data into forcing boundary conditions, on the one hand, and on the experimental verification of the predictive capabilities of these numerical models, on the other.

In this section, selected results from a prototype soil column, set up at the Structural Engineering Department of the Politecnico di Milano, and left in the environmental uncontrolled atmospheric conditions, starting from the end of October 2009, are presented. The prototype was designed to obtain direct experimental information on soil-atmosphere water exchanges, based on a simple measurement technology, which could be easily replicated in situ, when a true scale monitoring programme were planned. More details on the equipment and assessment of standard hydrologic models are provided by [Car11a, b].

2.2 Experimental Setup

The soil prototype cell (Figure 1) is a 1200 mm high transparent tube, made of acrylic to avoid any electrical interference with capacitive probes, with a 5 mm thick wall and an internal diameter of 290 mm. The column is fastened at its bottom into an acrylic base plate, by insertion in a 5 mm wide annular hole sealed with a couple of o-rings, to avoid evaporation or outflow of liquid water. The base plate internally allows for the allocation of a porous stone, eventually connected to an external water level regulation device and pressure measurement system. The diameter was chosen to ensure that the sensors response was not influenced by the wall of the acrylic tube. Previous experimental data had shown that the capacitive probes measurements are affected by the water content in a cylindrical volume of soil of about 160 mm diameter and 150 mm height, centred on the probe. At the centre of the base plate a 25 mm depth circular hole was designed, to ensure correct centred positioning of the capacitance probes PVC access tube.

To provide information on soil-atmosphere water exchange, capacitive probes were chosen. Suction was not controlled, nor measured, contrarily to what laboratory tests at the REV scale may suggest. This choice was dictated by the following reasons: (a) water content is the information needed for water balance evaluation, and (b) suction measurement in situ can be reliable only in a limited suction range, depending on the suction probes air entry-value, and on their response time.

Basically, the chosen probe provides the resonance frequency of an inductive-capacitive circuit, in which the soil participates as a resistive and capacitive element, depending on its water content. The sensor accuracy is ± 0.06% of the readout soil water content. A smaller-scale chamber had been previously designed to provide the reference data in water and in air, and to verify the calibration of the sensors inserted in a soil representative volume [Ava12].

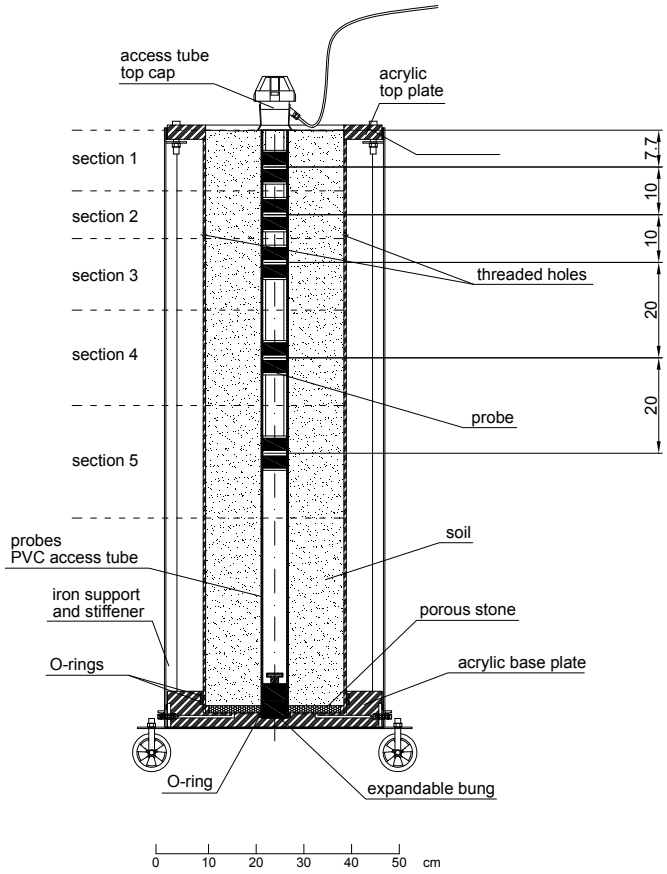

Figure 1: Schematic layout of the prototype column apparatus [Car11a].

A meteorological station, consisting of a rain gauge, a thermo hygrometer with an anti-radiant shield, a combined wind speed-direction sensor and a global radiometer was mounted nearby the prototype column, to provide actual meteorological information. The rain gauge has a resolution of 0.2 mm, with accuracy of ±0.2 mm/min in the range between 0 and 1 mm/min, and of ± 1% in the range 1-10 mm/min. The thermo hygrometer has accuracy of ± 0.1 °C for temperature, and of ± 1.5% for humidity. The wind sensor has a speed resolution of 0.05 m/s and a resolution of 4° for direction, a speed accuracy of 0.1 m/s ± 1% and a direction accuracy of 1% of the respective readout values. The global radiometer has an uncertainty of ±10% over a day measurement.

The installation depth of the five probes used in the prototype is indicated in Figure 1, and it was chosen in such a way that sharp gradients expected close to the soil-atmosphere boundary could be accurately tracked.

2.3 Experimental results

Data refer to a sandy silt, having a liquid limit of $w_L = 0.33$ and a plastic limit of $w_P = 0.20$. The soil was mixed with tap water, left to homogenise in a humid chamber for 24 hours, and then compacted as uniformly as possible in layers of 10 cm thickness. The as compacted mean void ratio was $e_0 = 0.55$ at an initial degree of saturation $S_{r0} = 0.50$.

Meteorological data measured in the first two months, from 20/10/2009 to 20/12/2009 are reported in Figure 2, while the response of the soil water probes is collected in Figure 3. In the figure, the probes data are already processed to give the volumetric water content time evolution at the various depths. Soil water content was registered any 5 min, while the weather parameters were collected every 20 min.

The data allow for distinguishing clearly the response of the soil to the forcing meteorological conditions, and to highlight the role played by the soil hydraulic properties and by the previous hydraulic history. The progression of infiltration fronts following rainy events may be appreciated by the sudden increase of the water content, with a time lag increasing from the top to the bottom of the soil column. Equally, the evaporation rate tends to decrease with depth, and can hardly be appreciated below the first 50 cm depth.

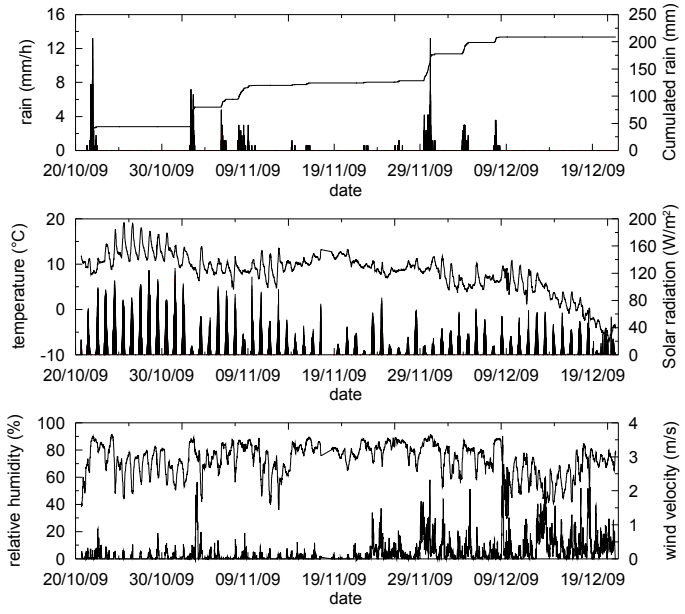

Figure 2: Meteorological data [Car11a].

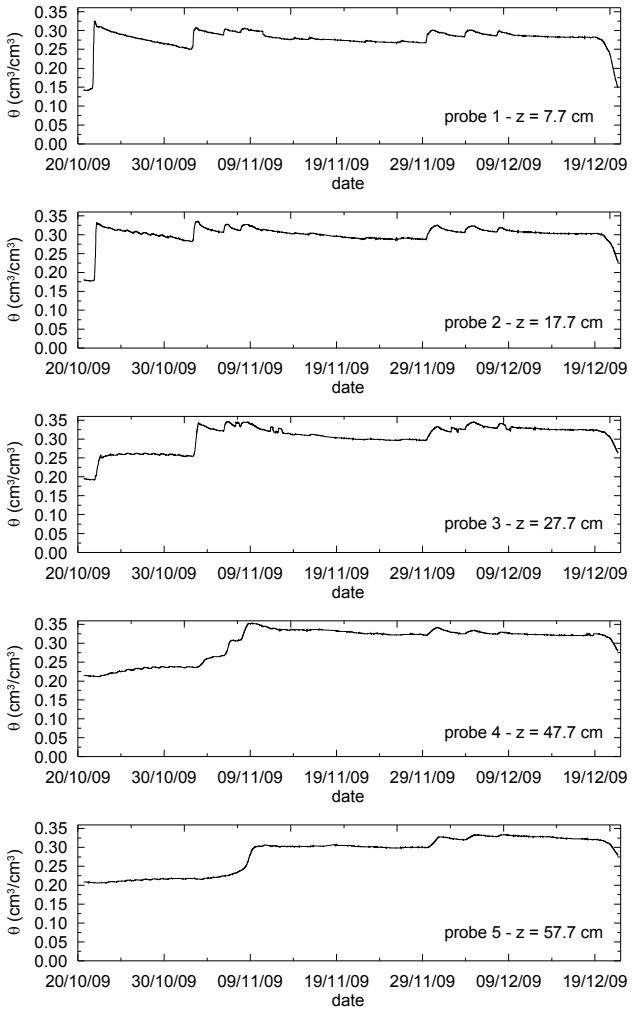

Figure 3: Evolution of soil volumetric water content at increasing depths [Car11a].

Immediately after rain stops, in the upper portions of the soil the water content starts to decrease at a rate which seems to be independent from the actual temperature or relative humidity. The datum suggests that, for this soil, the dominating process just after a rainy event is downward infiltration, at least for a short time interval. Afterwards, the water content variation tends to stabilise to a constant decreasing rate, which is interpreted as the effect of evaporation towards the upper surface. Only the first 50 cm topsoil seem to contribute significantly to the evaporation process, although a slight decrease in the water content at a depth of 57.7 cm begins to be appreciated when the actual saturation degree is close to one.

To provide deeper insight into the soil water mass balance, three rainy events are analysed in more detail. The first one had a cumulated rain of 43.8 mm in about 11 hours (Figure 4), the second one 36 mm over a 14 hour period (Figure 5) and the last one 47.6 mm over 22 hours (Figure 6). In each figure, the probe readings and the rainfall event description (intensity and cumulated values) are reported, together with diagrams which help in the analysis of water balance. To perform the balance, the column was subdivided into five sections, starting from the top soil-atmosphere interface (Figure 1). Volumetric water content measured by each probe was assumed to be representative of the whole section. The incremental and the cumulative mass variations were then calculated starting from the top section and adding progressively the underlying layers.

The data referring to the first event (Figure 3) clearly show the advancing front starting from the first section and reaching the third section after few hours. Sections 4 and 5, below the first 30 cm, are not affected directly by the rain event. The amount of water which can be stored in the upper layers correspond to the difference between the water content at the beginning of rain and the water content corresponding to saturation. Once saturation is reached, the probe reading remains constant until rain stops. Constant readings in the upper soil layers at increasing water content at greater depths denote a continuing infiltration process downwards. The cumulative mass variations in the first sections show that all the rain infiltrates into the soil, due to the initial low water content.

Infiltration following the second rainy event analysed (02/11/09, Figure 4) reaches more rapidly the third section and starts to affect also the lower section 4. Nonetheless, the amount of water stored into the soil layers is still measured by the water content variation in the first three sections. In fact, when the fourth probe reading starts to increase (at the beginning of the day after the rain), in the upper layers the water content is already decreasing, denoting that a downward redistribution process is taking place. The amount of water that infiltrates into the soil is less than that available from rainfall, even if the cumulated rain is lower than in the previous event and its duration is longer, which is a clear consequence of the role played by the initial soil water distribution.

The influence of the initial water content distribution is even more evident with reference to the third rainy event (Figure 5), characterised by a cumulate similar to the first one analysed, albeit distributed over a longer time period. In this case, the infiltration front clearly reaches quickly the last monitored section, as the upper layers were close to saturation already at the beginning of the rainfall. Nonetheless, only one third of the total amount of water available from rainfall infiltrates into the soil, as the peak in the cumulative water mass shows, just at the end of the rainfall. In this case, water ponding was clearly evident at the top surface.

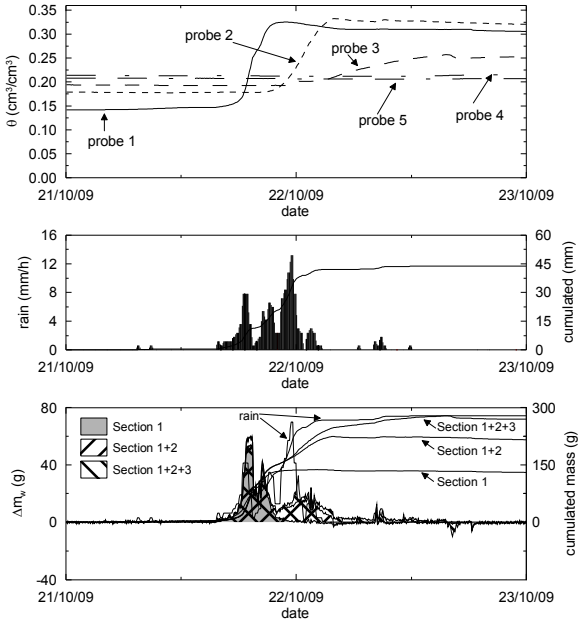

Figure 4: Data and elaborations for rainfall event on 22/10/2009 [Car11a].

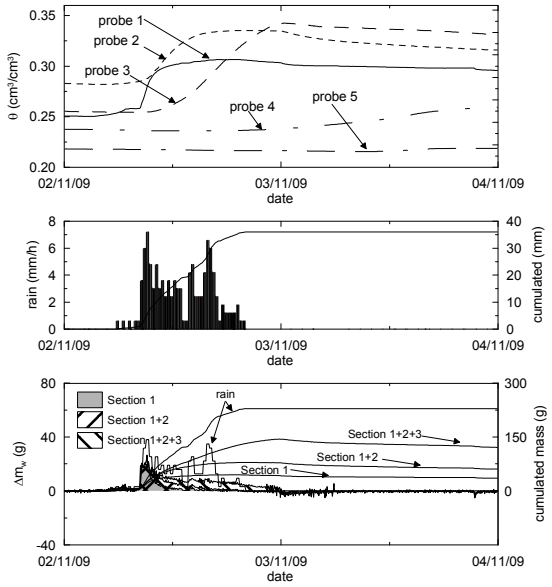

Figure 5: Data and elaborations for rainfall event on 2/11/2009 [Car11a].

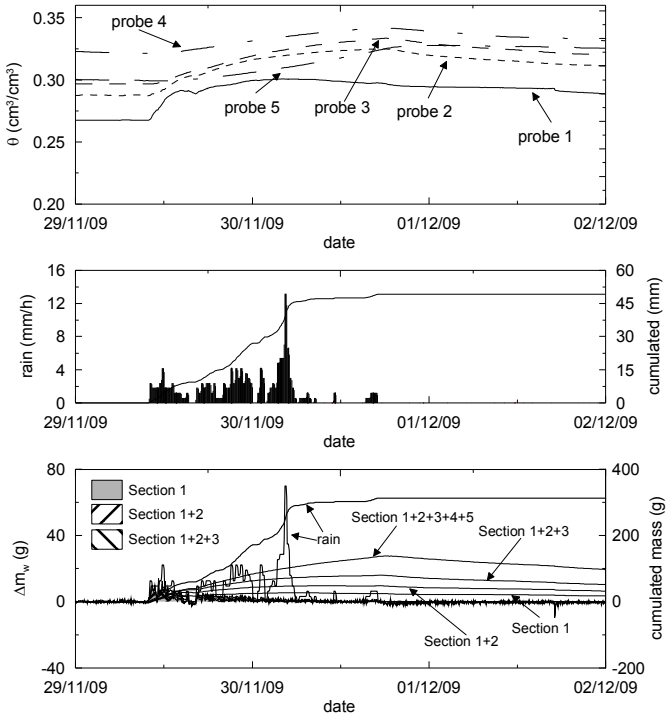

Figure 6: Data and elaborations for rainfall event on 29/11-30/12/2009 [Car11a].

The previous three comparisons highlight that in real problems, when coupled transport processes occur in the field – which is simulated in the prototype column – different aspects concur to determine the soil response, which is not homogeneous at all, in spite of possible homogeneity of soil properties. Not only non-linear coupling affects the behaviour of the soil at the REV scale, as already discussed in the previous chapters, but also the local actual state of the soil at the beginning of any event largely determine the soil response. Here, water saturation distribution at the beginning of rainfall events clearly emerged as the key factor in the water balance, given the soil properties and the forcing boundary conditions. Internal redistribution takes place continuously and affects increasing depths as the average water content increases.

In practical applications, not only the boundary conditions cannot be controlled, but also the response of the soil is dynamically evolving as a function of the actual boundary conditions and of the previous loading history, which cannot be completely reproduced at the scale of a laboratory test. The prototype soil column apparatus, developed for the analysis of soil-atmosphere interaction, allows for tracking water balance depending on rain infiltration, evaporation outflow and moisture movements inside the soil, but only by careful post processing of the soil water content data.

The soil column was instrumented with capacitive probes only, in view of the field applications, where the installation of other measuring instruments would be more difficult or less significant. Although suction probes would provide a more complete picture of the hydraulic state of the soil, their response time is much higher than that of water content probes, whenever installed in soils finer than sands.

3 Thermo-hydraulic boundary value experiments

3.1 Thermo-hydraulic properties using simple setups. Back-analysis of parameters

A simple testing setup was developed by [Pin02a,b] to determine selected thermo-hydraulic parameters on heavily compacted Febex bentonite under partially saturated states. Tests were designed to apply a controlled flux of heat at one of the ends of a cylindrical specimen (38 mm diameter, 76 mm high) and to maintain the other end at constant temperature. A latex membrane allowed soil deformation while keeping constant the overall water content. Since coupled phenomena could induce flow of water either because of pressure gradients (liquid flow) or because of vapour diffusion, local water contents were expected to change inside the sample. An additional external layer (55 mm thick) of heat insulating deformable foam surrounded the specimen, to limit lateral loss of heat. To ensure well reproducible boundary conditions and a controlled heat flux at the sample ends, two identical parts of specimen were placed symmetrically to the heater, as shown in Figure 7. The heater is a copper cylinder (38 mm diameter, 50 mm high) with five small electrical resistances housed inside. In the tests, a constant power of 2.6 W was used, which allowed reaching steady state temperatures in the range of 70-80ºC at the hotter end of the specimen. At the colder end, a constant temperature of 30ºC was maintained by circulating water through the stainless steel head in contact with the soil (Figure 7).

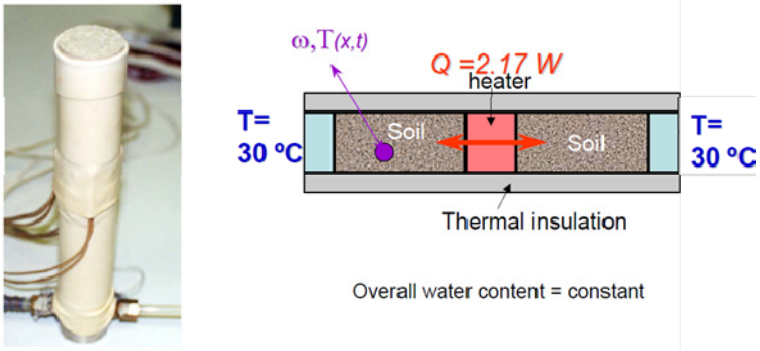

Figure 7: Photograph of the simple experimental setup (without external thermal insulation and upper head) and scheme of the experimental device [Pin02a,b].

During the tests, temperatures at both ends and at three internal points of the specimen, located at regular intervals, were monitored. At the end of the tests, the soil samples were cut into six small cylinders and the water content of each one determined.

Three specimens of bentonite statically compacted at a dry density of 1.68 Mg/m^3 and with initial water content of 15.3, 16.9 and 17.1%, respectively, were tested. Temperatures measured during the heating period for one of the specimens (w=17.1%) are shown in Figure 8. Temperature reached a quasi-steady state regime after 10 hours.

A back-analysis procedure was used for the identification of some thermal and hydraulic parameters [Pin02a]. The fully coupled finite element program Code_Bright [Oli96] was used to model the thermo-hydraulic behaviour of the clay. Axisymmetric analyses allowed evaluating the effect of loss of heat at the lateral boundary of the sample –around 60% of total heater power–, which highlighted the importance of performing 2D analyses of the experiment, instead of more simple 1D simulations.

Temperatures obtained at four different elapsed times and at four points of the sample, as well as water contents measured at the end of the test, were considered as data vector for the inverse problem. Optimisation aimed at reducing the value of an objective function, expressing the difference between values predicted by a forward model of the test and data vector. For each test, optimisation was achieved by changing the value of three model parameters. Among these, one corresponded to the thermal problem –the thermal conductivity of bentonite under saturated condition, λ_{sat}–; and two corresponded to the hydraulic problem –the tortuosity factor τ affecting the diffusion of vapour [Oli94], and the exponent β of the unsaturated relative permeability law (k_r=S_r^{β}). The remaining model parameters were obtained directly from complementary tests [Llo07]. The values of β, τ and λ_{sat} found are summarised in Table 1.

Table 1: Exponent in relative permeability law obtained for the different tests.

Test	Water content (%)	β in $k_r = S_r^{\beta}$	Tortuosity factor τ for diffusion of vapour	Saturated thermal conductivity λ_{sat} ($Wm^{-1}K^{-1}$)
1	15.5	3.06	0.56	1.19
2	16.9	1.10	0.74	1.31
3	17.1	1.68	0.90	1.38

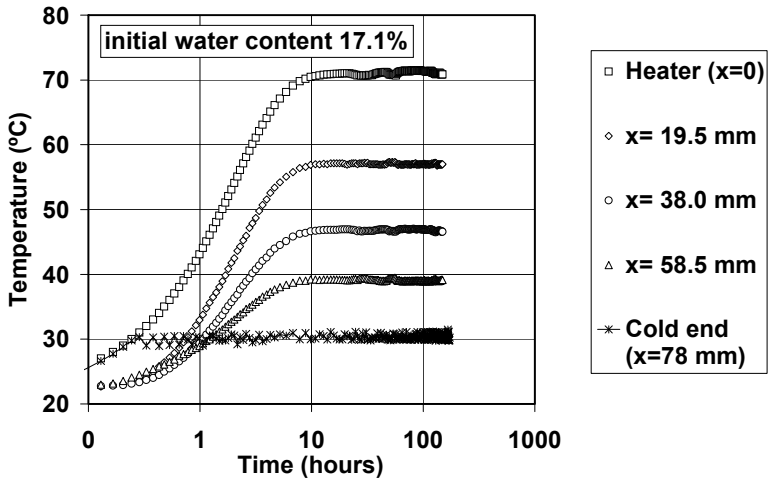

Figure 8: Evolution of temperature in a prescribed heat flow test [Pin02b].

The optimisation procedure showed that there were different combinations of parameters giving equivalent results in terms of the objective function. This was expected, since in the measured water content it was difficult to distinguish between water transported by liquid flow (controlled by β) and by vapour diffusion (controlled by τ). Taking into account all the tests together, the following set of parameters and laws was selected:

$$k_r = S_r^3 \;;\quad \tau = 0.8 \;;\quad \lambda\,(\mathrm{Wm^{-1}K^{-1}}) = 0.47 + 0.68 S_r \tag{1}$$

This set of parameters was used to solve the direct problem and simulate all the heat flow tests, which are plotted in Figures 9 and 10. The error between measured and computed values was of the order of magnitude of the measurement error [Pin02b]. As observed in the figures, the inverse method provided a systematic and consistent procedure to find the best parameters that reproduced the measurements for the selected model. The method also gave further insight into the model by allowing capturing the dependence and coupling between parameters [Pin02b].

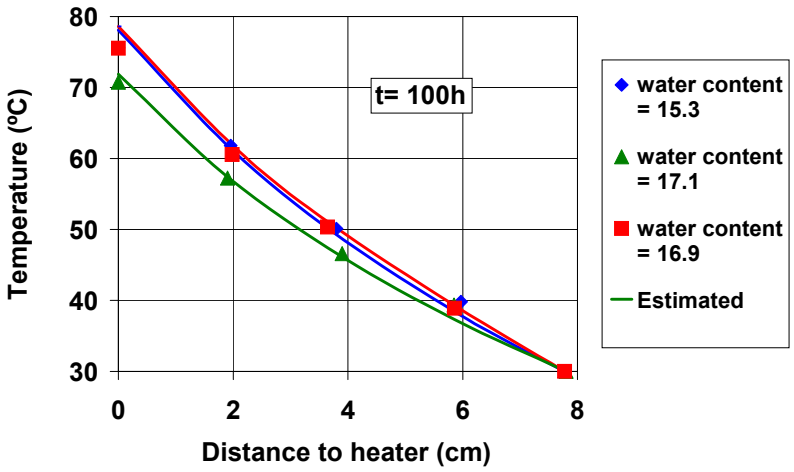

Figure 9: Measured and computed temperatures in the prescribed heat flow tests, using the final selected parameters [Pin02b].

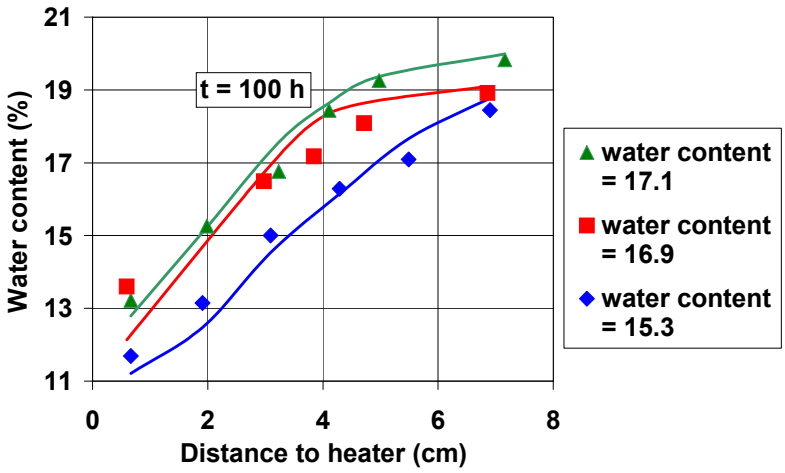

Figure 10: Measured and computed water contents in the prescribed heat flow tests, using the final selected parameters [Pin02b].

3.2 Constant volume cell for heating pulse tests. Experimental setup, back-analysis of thermal parameters and simulation of results

Thermal impact may play an important role on the behaviour of low-permeability saturated clayey formations in connection with the design of a repository for 'High-Level Radioactive Waste'. This impact can be studied through back-analysis of heating pulse tests.

Figure 11 shows a scheme of a constant volume (isochoric) and axi-symmetric heating cell [Muñ09, Lim10, Lim11], which is used to study heating pulse tests with controlled power supply and controlled hydraulic boundary conditions. Soil sample size is 75 mm in diameter and 100 mm high. A controlled-power heater is installed along the axis of the sample in the lower part of the cell. Different transducers monitor the sample response, as shown in the figure: two miniature pore water pressure transducers (Pw_1 and Pw_2 in Figure 11), and three thermocouples (T_1, T_2 and T_3). The cell is equipped with top and bottom valves to apply controlled hydraulic boundary conditions (u_u and u_b).

Heating tests at (nearly) constant volume and different target temperatures (maximum 85°C) were performed under controlled hydraulic boundary conditions on natural and saturated Boom clay [Lim10, Lim11]. Attention is focused on the time evolution of temperature and pore water pressure changes during heating and cooling paths –i.e., pore pressure build-up during quasi-undrained heating and later dissipation to the applied hydraulic boundary conditions–. Throughout the course of the heating/cooling paths, the bottom drainage is maintained open at constant water backpressure using an automatic pressure / volume controller, while the upper valve is kept closed. This backpressure is important since it allows measuring the pore pressure drop during the cooling phase without invading the negative range (below atmospheric conditions). The initial and external temperatures are regulated by submerging the cell inside a temperature controlled water bath at temperature T_4 (Figure 11). Figure 12a shows the time evolutions of temperature for different locations and along a heating and cooling cycle. Figure 12b presents the corresponding time evolutions of pore water pressures.

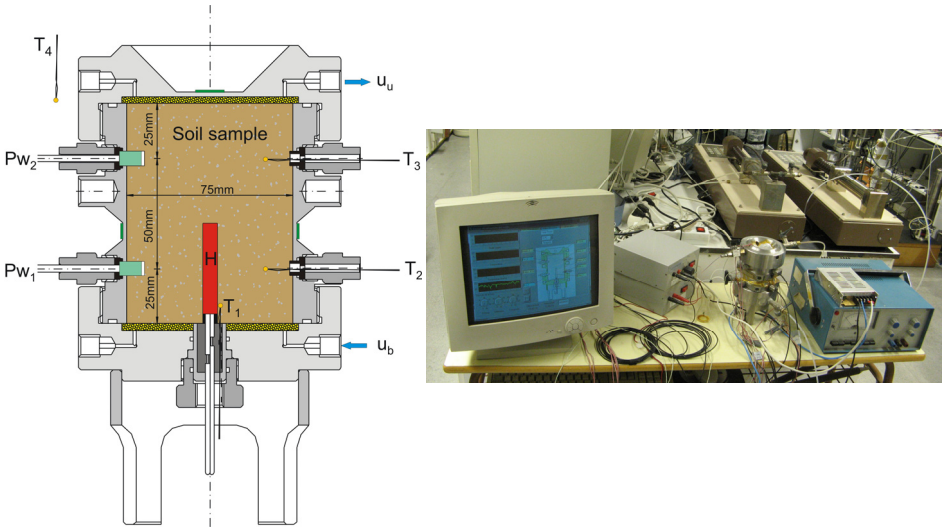

Figure 11: Quasi-isochoric axi-symmetric heating cell and components [Lim10, Lim11].

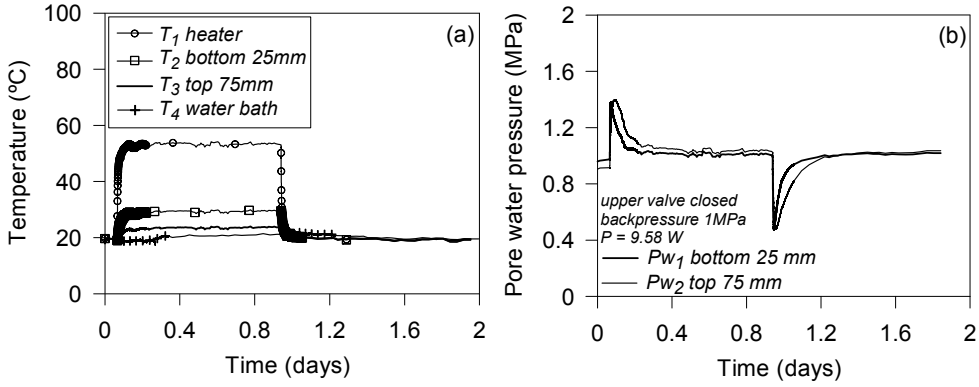

Figure 12: Temperature and pore water pressure evolutions during heating and cooling paths on saturated Boom clay [Lim10, Lim11].

In the interpretation of the test results, it was assumed that temperatures and heat flux were not influenced by water pressure and flow, which means that heat convection was assumed to be negligible. The driving process for temperature change during the test is thus conduction only. This assumption is justified by the condition of constant overall volume prevailing in the heating cell that makes the change in porosity and the velocities of the solid phase very small. Moreover, the low permeability of the material prevents the existence of high velocities for the liquid phase. The flux of heat convected by the solid and liquid phases is, therefore, extremely low.

On the contrary, water pressure and flow were assumed to be influenced also by temperature: as a consequence, while the thermal problem was decoupled from the hydraulic one, the hydraulic problem was coupled to the thermal one.

The test was then interpreted in two separated stages. First, a back-analysis of temperature measurements was carried out by performing uncoupled thermal simulations using the finite element program Code_Bright [Oli96]: only the balance equation for energy was solved. Heat exchanged by the highly conductive stainless steel cell with the controlled water bath was accounted for as a convection-type boundary condition of the problem. This heat flux was assumed to be proportional to the difference between the temperature of the cell and the temperature of the water bath (around 19ºC) at each boundary node, through a convection coefficient h. Thermal optimisation was then aimed at identifying the values of the saturated thermal conductivity λ and the convection coefficient h. Calculations were performed for different combinations of λ and h. For each of them, a measure of the discrepancy between temperature simulation results and temperature experimental measurements ε was computed for different elapsed times. The three-dimensional plot in Figure 13 shows the differences ε between simulation results and experimental observations. The best agreement was obtained for $\lambda = 1.6$ $Wm^{-1}K^{-1}$ and $h = 24$ $Wm^{-2}K^{-1}$. Figure 14 (at the bottom) displays the temperature field inside the cell at the maximum temperature of the heater (85ºC) and under steady state conditions and using the previously back-analysed parameters.

Thermal parameters were then further used to calibrate selected hydraulic parameters by analysing joint thermal and hydraulic results. Figure 15 displays the time evolutions of temperature and pore water pressure (experimental and simulated results) of Boom clay during heating and cooling paths. The water permeability values determined by back-analysis were in agreement with direct measurements performed with controlled-gradient tests.

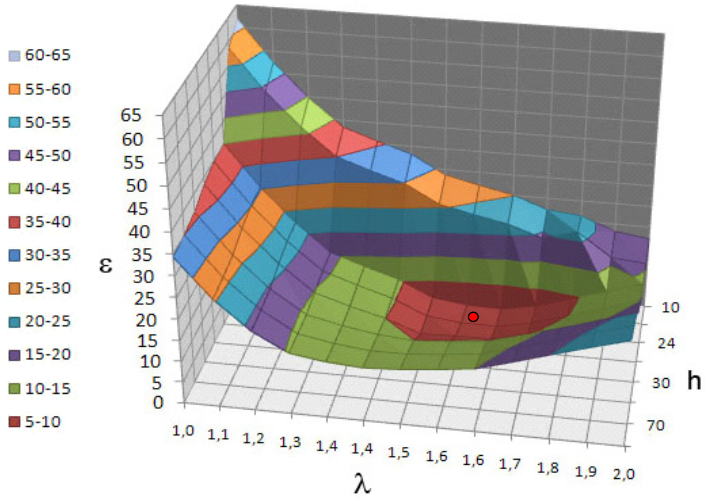

Figure 13: Three-dimensional graph showing the differences in temperature between observations and calculations in the back-analysis of the heating pulse test. Determination of thermal conductivity λ and convection coefficient h [Lim11].

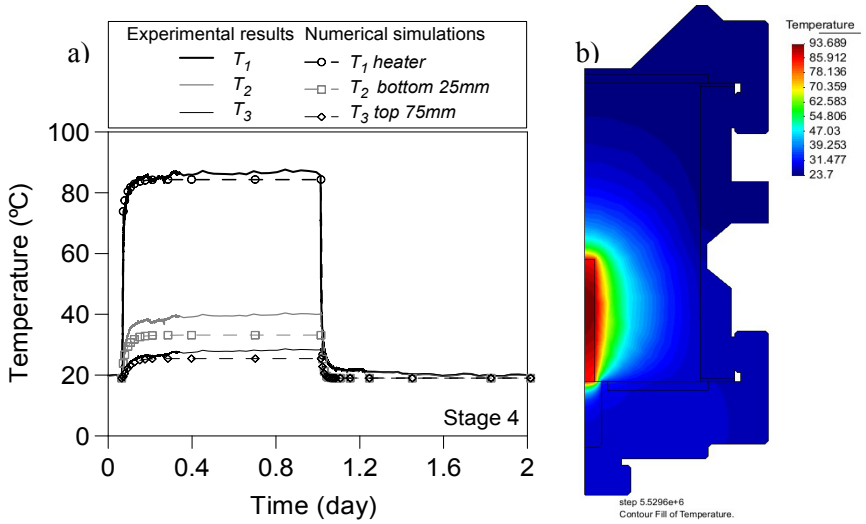

Figure 14: (a) Time evolution of temperature: experimental and simulated results. (b) Temperature field inside the cell at maximum heater temperature [Lim11].

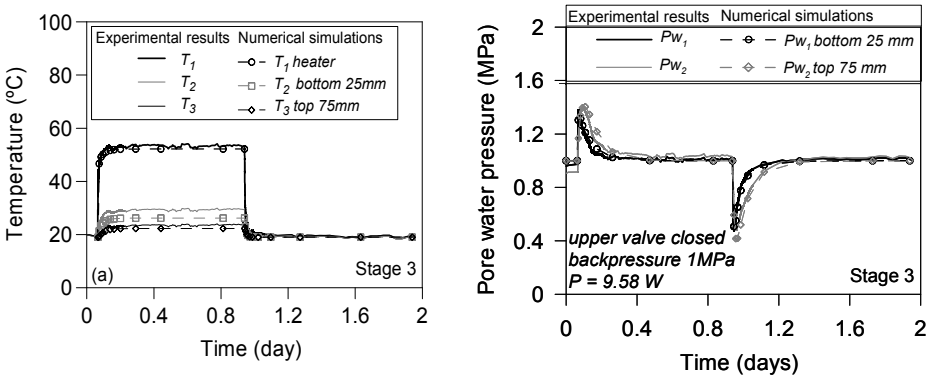

Figure 15: Heating and cooling paths on Boom clay. Experimental and numerical results [Lim11].

4 Air tests on low-permeability claystone formations

Understanding the phenomena and processes associated with release of gases from the disposal systems of a geological repository for radioactive waste is one of the key issues in the assessment of repository performance [Hor99, Har03, Arn08]. The actual gas migration mechanisms may entail standard two-phase flow conditions (partially displacing water) or more complex mechanisms involving coupled two-phase geomechanical phenomena –in all cases, preferential gas pathways will develop taking advantage of the material heterogeneity and anisotropy, rock discontinuities or interfaces–. These gas transport mechanisms are sensitive to the stress state. In fact, two-phase flow is affected by porosity changes and pathway transmissivity is sensitive to fracture aperture variations (see for instance, [Oli08]). Laboratory scale experiments under controlled pneumatic, hydraulic and mechanical boundary conditions are important within this context to provide quantitative data for model validation (applicability of two-phase flow models) and for parameter estimation (calibration of hydraulic and two-phase flow properties).

Figure 16 shows a scheme of the high-pressure triaxial cell jointly with the test set-up, which was specifically designed to apply isotropic/anisotropic stress states up to a maximum of 40 MPa, while injecting air at controlled volume rate [Rom10, Rom12a,b]. Axial strain of small-height specimens –confined by several neoprene membranes and aluminium foils– is registered by an external LVDT transducer. Each cap of the triaxial cell has inlet and outlet lines, prepared for gas and liquid connections. The equipment uses four automatic pressure / volume controllers (P/V in the figure), two for gas (injection and extraction at downstream point), and two for water, which can be used in combination (for example, air injection and water pressure at downstream). The gas injection pressure / volume controller has a maxi-

mum range of 20 MPa (maximum volume 500 mL), and is able to control volume rates between 10^{-4} mL/min and 100 mL/min (volume resolution < 5 mm^3). The 2 MPa P/V controllers for air and water at downstream present a volumetric resolution of 1 mm^3 (pressure resolution 1 kPa).

Before the air injection tests, saturation of the samples was ensured, and water permeability was measured using different hydraulic gradients at different isotropic confining stresses. Figure 17 displays a scheme of this type of hydraulic test (test A in the figure), in which upstream / downstream volume changes and axial strains are recorded. For the air injection test B in the figure, the upstream water line was rapidly drained to inject air pressure at 0.5 MPa and the recovery system maintained with water at 0.5 MPa to better ensure sample saturation. The sample was let to equalise under an initial pore water pressure of 0.5 MPa and at the target total stress (typically between 15 and 19 MPa). Fast air injection at controlled volume rates (typically at 100 mL/min) started from an initial air pressure value of 3 MPa. After reaching maximum air pressure (lower than the confining stress), the upstream piston was stopped and air pressure was let to decay at constant volume. Fitting the constant mass system for different injection periods allowed estimating the initial injection volume of air (injection piston and air lines). Pressure deviations from the perfect gas law for a constant mass system in the injection point allowed estimating the injected mass of air and mass inflow rates into the sample. Information on outflow rates was recorded and used to define the breakthrough pressures.

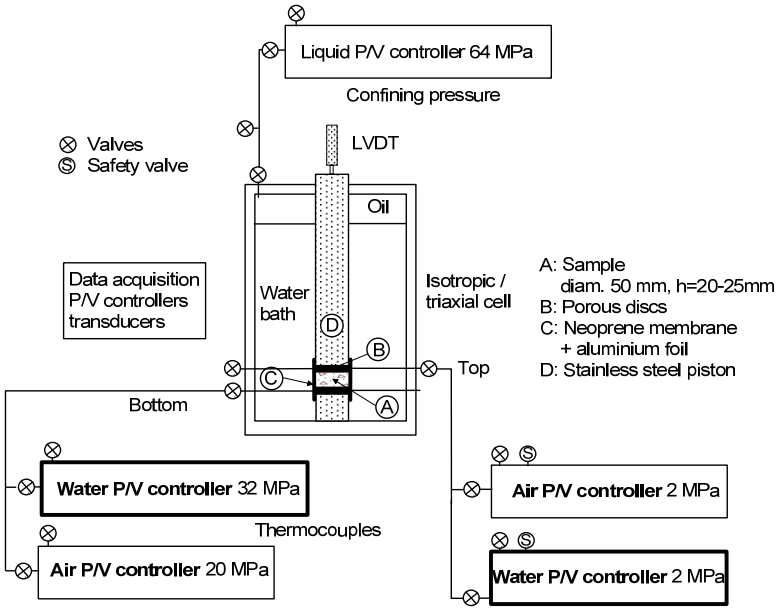

Figure 16: Scheme of the air injection and water permeability setup with high-pressure triaxial cell and four pressure/volume controllers (two for air and two for water) [Rom12a,b].

Figure 18 shows the time evolution of air injection pressure during a fast controlled volume-rate test at 15 MPa isotropic confining stress on a low-porosity claystone sample. V_0 in the figure represents the initial injection volume of air (injection piston and air lines). As observed in the figure, the injection pressure increased up to 13 MPa, followed by a shut-in and recovery period at constant volume. Outflow response was immediately observed after shut-in corresponding to a small drop in the injection pressure, followed by a subsequent gradual decline. After the apparent air breakthrough process –corresponding to an increase in the outflow pressure–, the injection pressure showed a steep decline. The constant downstream pressure condition of 0.5 MPa was not possible to maintain due to the high outflow volume rates detected (the downstream pressure increased until reaching 2 MPa, where a constant pressure was again prescribed by the pressure release valve). With regard to the axial displacement response (negative axial displacement corresponds to expansion), the sample at constant isotropic total stress displayed quasi-reversible features with expansion at the early fast air injection stage and progressive compression towards approximately the initial volume on air pressure dissipation.

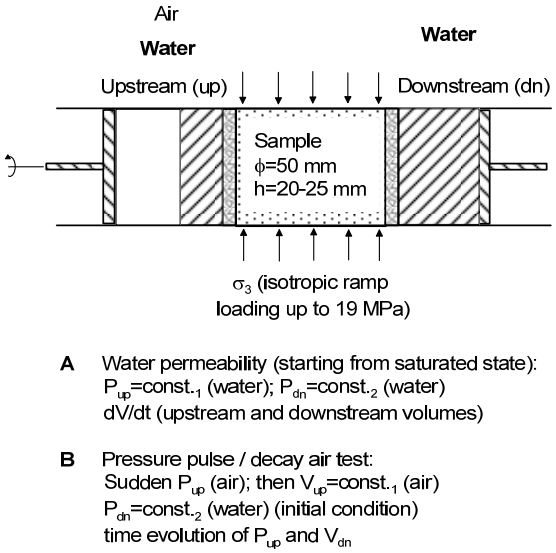

Figure 17: Type of tests performed during controlled-gradient water permeability tests and fast air injection tests followed by recovery period at constant volume [Rom12b].

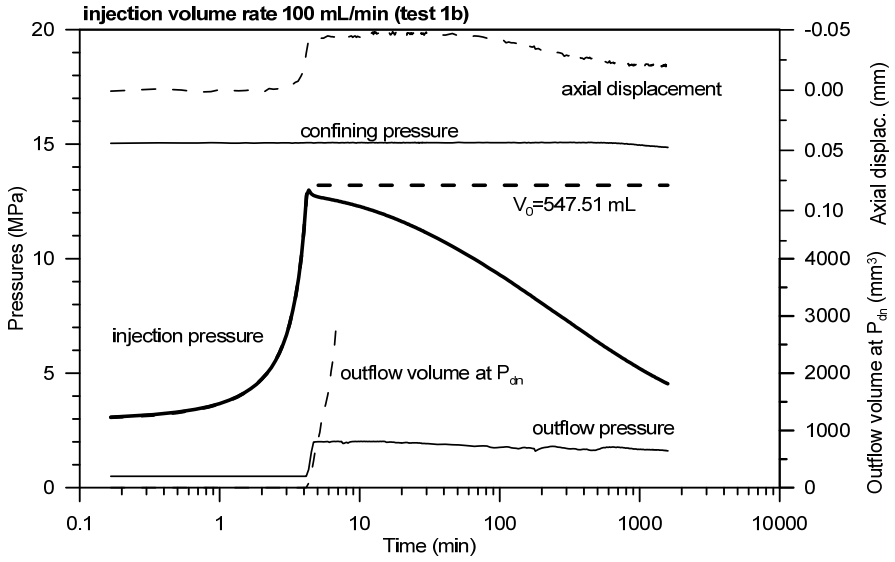

Figure 18: Measured time evolution of pressures at the injection and outflow sides together with outflow volume and axial displacement [Rom12a,b].

To help with the interpretation of the results and for the investigation of the measured responses in terms of injection and outflow pressures, as well as outflow volumes, numerical models were used implementing the geometry of the sample and the corresponding boundary conditions on the injection and outflow sides. For the analyses, standard two-phase flow processes were considered in the numerical model in an attempt to reproduce the observed measurements. The two-phase flow code TOUGH2 [Pru99] was used, which takes into account fluid flow in both liquid and gas phases occurring under pressure, viscous, and gravity forces according to Darcy's law. Pressures in the liquid and gaseous phases are related by the capillary pressure functions and interference between the phases is represented by relative permeability functions. Standard two-phase flow model parameters were calibrated based on the experimental data, as well as by inverse modelling of the air injection / outflow responses using ITOUGH2 code [Fin07]. Results of the numerical modelling are shown in Figure 19, together with some of the estimated two-flow phase parameters (intrinsic permeability K, and parameters p_0 –associated with air-entry process– and n of the van Genuchten model used for the water retention curve [van80]).

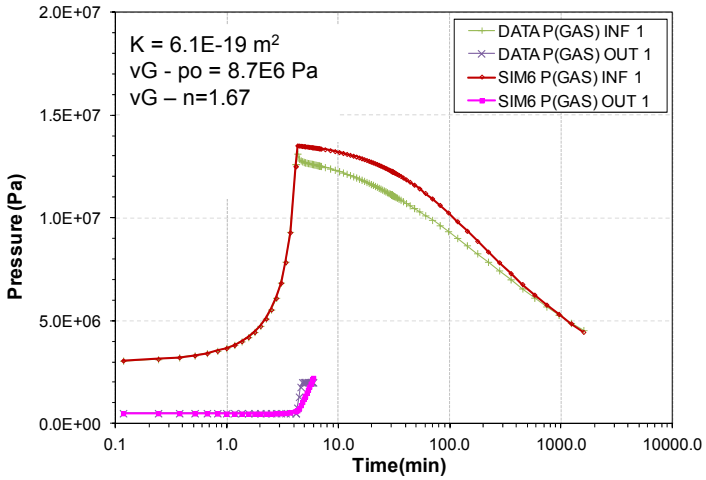

Figure 19: Simulation (sim) and measured (data) results in terms of injection pressure and outflow pressures [Rom12b].

As observed in Figure 19, the analysis using standard two-phase flow model provided insight into the overall air flow mechanisms and showed a good agreement between the measured pressures at the injection and outflow sides of the sample. However, no consistent parameter set could be determined, in agreement with the complementary characterisation tests performed on the material, which can be attributed to the compressibility of the sample and the resulting non-linear phenomena (changes in porosity along the sample). Changes in porosity associated with changes in constitutive stress and corresponding changes in intrinsic permeability have not been considered in the present study. Numerical analyses are currently being performed [Sen12] that include the coupled changes in porosity and intrinsic permeability under changing stress states, hence accounting for coupling between pore compressibility, porosity, intrinsic permeability and capillary pressure.

5 Monitoring processes with ERT

5.1 Introduction

Although ERT has a lower resolution than other techniques (e.g. X-ray tomography, [Ols99]), it can be convenient since it is relatively easy to implement, flexible and economic. ERT has been used to monitor: transport of saline tracers [Bin96, Dam09, Com11, Pol12], mechanical consolidation [Com10] and unsaturated flow [LaB04, Cos12, Bre12], in both two dimensional and three dimensional conditions.

Monitoring is made through of a sequence of maps of electrical conductivity obtained through ERT reconstructions. Transport phenomena can be visualised as a

series of 'electrical pictures'. The effects of material or pore network heterogeneities on transport can be appreciated. For instance, by plotting electrical conductivity histories at selected points, [Bin96] showed areas of preferential flow on a planar section of a flow column.

3D ERT analysis of hydro-chemo-mechanical processes can be done with experimental cells such as the 'EIToedometer' described in [Com08], an oedometer cell whose sidewall and top and bottom plates are covered with a plastic insulating material (Figure 20). Electrodes are both on the sidewall of the cell and on the top and bottom plates. Measurement protocol can then include 'horizontal' measurements, in which the pairs of electrodes that apply electrical current and those that measure electrical potential are on the sidewall; 'vertical' measurements, in which both types of electrodes are on the base and top plates; and 'mixed' measurements, in which the electrodes that apply electrical current are on the sidewall and the measuring electrodes are on the plates. Other 3 D cells such as those of [Ols99, Koe08] have electrodes only on the sidewalls, but at different heights.

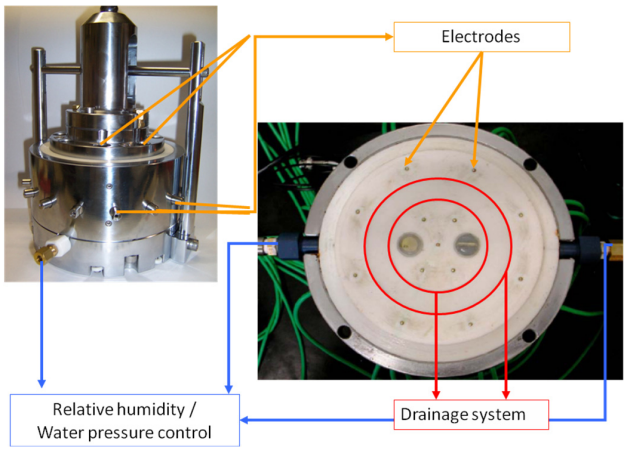

Figure 20: Pictures of the EIToedometer described in [Com08] evidencing the position of the electrodes and the drainage system. The cell diameter is D=130 mm while the cell height can range from H = 40 mm to H = 60 mm.

Time needed to run a complete set of measurements necessary for a single 3D ERT image is highly dependent on the system used (number of electrodes, number of measurements, operating frequency). Anyway it is generally short compared to characteristic times of most hydro-chemo-mechanical processes studied in the laboratory. As an outcome, for monitoring and back-analysis purposes, it is legitimate to associate each image with a well defined time instant.

Transient processes can be imaged as local changes of electrical conductivity. Due to intrinsic heterogeneity of samples, when the perturbation caused by transient

processes is small, appreciating small electrical changes caused by testing can be difficult. Visualisation in terms of differential images can be convenient. In differential images the difference between the electrical conductivity at two given moments is plotted, so that the effects of transient processes are emphasised.

Figure 21a refer to the analysis of a consolidation process occurring in the EIToedometer [Com10]. The difference between the electrical conductivity immediately before imposing a load and the electrical conductivity while consolidation is ongoing is plotted here. A threshold in the representation ($\Delta\chi$ = 0.001 mS/ cm) has been set to evidence the zones of the sample where larger electrical conductivity changes have taken place. Since chemical composition was maintained constant throughout the test, detected conductivity changes are related only to porosity reduction. Actually, volumes where this phenomenon is more relevant merge towards the drainage lines.

Figure 21b is an example of detection of flow patterns [Com11]. It refers to a sample where a layer of kaolin (10 mm thick) was placed between two layers of sand (15 mm thick each). NaCl grains were placed on top of the upper sand layer and wetted to induce dissolution and transport through the cell. The electrical conductivity increase, plotted in Figure 21b, can then be interpreted as an increase of NaCl concentration within the pore water. The differential image shows the difference between the electrical conductivity 60 minutes after the beginning of the test and the initial one. Salt concentration increased in the upper sand layer and also at the interface between kaolin and the cell walls. Thus, the image testifies a weak contact between the kaolin layer and the cell and a preferential flow path for salt.

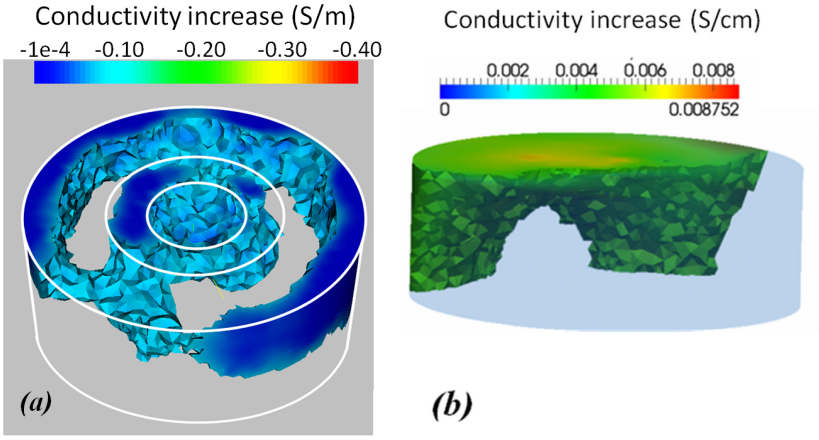

Figure 21: (a) 3D ERT differential image of mechanical consolidation. Porosity reduction (conductivity loss) close to the drainage lines is evident; (b) 3D ERT differential image of salt transport. Zones of increased salt concentration (higher conductivity increase) show migration of salt through a weak contact zone between kaolin and cell wall.

5.2 Back-analysis of transport processes with ERT

Use of ERT reconstructions for back analysis of transport processes and parameter estimation has been developed firstly for in situ geophysical applications [Mic03, Sin05] and then for laboratory experiments [Koe08, Cos12, Pol12]. Several field tests showed so called 'mass balance problems', i.e. significant differences between the total mass of water (or salt) actually present in the monitored domain and the mass estimated via ERT reconstruction. For instance while monitoring an infiltration test [Bin02] found that the increase in the amount of water estimated by the ERT was consistently lower than the real amount, with errors up to 50%. Errors such as this have generally been attributed to poor resolution of the electrical measurements in areas far from the electrodes and to smoothing, together with the fact that boundary conditions associated with the hydro-electrical problem are not univocally established during field tests [Koe08]. Mass balance problems, that can prejudice success of back-analyses, have not been detected in recent laboratory experiences [Koe08, Cos12] (Figure 22).

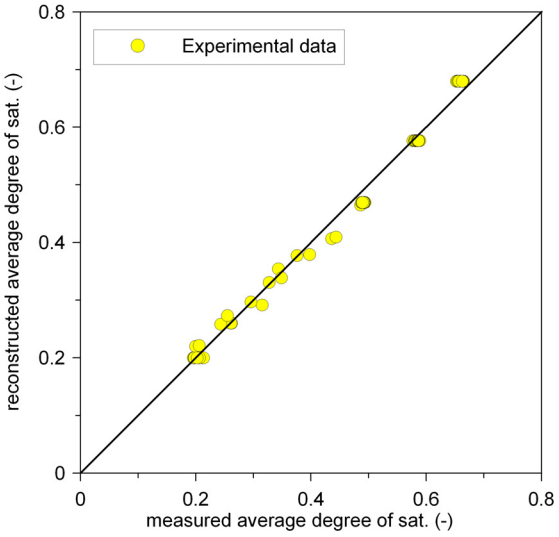

Figure 22: Mass of water detected through ERT inversion (expressed in terms of saturation degree) compared with mass of water actually present in the sample [Cos12]. The sample had an initial saturation S_r=0.2 and was then wetted under controlled flow conditions.

Both *decoupled inversion* and *coupled inversion* strategies have been implemented for back analysis. *Decoupled inversion* requires two different reconstruction stages. The first reconstruction refers to the electrical problem: electrode measurements at the boundaries are the data vector and reconstruction provides a map of estimated local conductivities. These conductivities are converted into water content / water concentration. In the second reconstruction the water content / salt concentration

maps obtained through the first inversion are used as data vector. The forward model is the hydro-chemo-mechanical model of the problem of concern and optimisation is obtained by changing its parameters.

Coupled inversion requires a single inversion process. Archie's law, the mass balance equation(s) of the hydro-chemo-mechanical problem and the electrical charge balance equation are coupled together since the beginning. Data vector is populated by the electrode measurements, while minimisation is done directly on the hydro-chemo-mechanical parameters. Decoupled inversion can suffer from the presence of artefacts and smoothing effects of ERT inversion, while coupled inversion can be computationally demanding and then strategies can be introduced to reduce the complexity of the problem (e.g. [Pol12]).

Decoupled inversion has been used by [Cos12] to estimate the parameters of the water retention curve (wetting branch) of sand and silt samples. Samples were placed in the EIToedometer (moist tamping) at an initial saturation degree Sr=0.20 and wetted by imposing a constant water pressure at the bottom end of the sample. Fast (type 1) and slow (type 2) wetting tests were run on both materials. In the type 1 tests, the imposed water pressure was 50 kPa : after about 1 minute of water inflow, drains were closed and electrical measurements were performed at a constant global water content for 3000 minutes to assess the local redistribution of water (homogenisation). In the type 2 tests water pressure at the boundaries was 5 kPa, applied for about 40 minutes. Electrical measurements were performed during wetting and homogenisation.

Figure 23 shows the evolution of electrical conductivity over time in a longitudinal section of the sand sample, under 'fast' wetting conditions. Time t=0 (Figure 23a) corresponds to the initial condition, consisting of a homogenous electrical conductivity field. Water inflow took place after the ERT reconstruction shown in Figure 23a and was already completed by the time of occurrence of the ERT reconstructions presented in Figures 23b, c and d.

Changes in shape and tone of darker areas in Figure 23 are associated with movement of water. Since wetting was 'fast', in Figure 23b the water content close to the drainage system is higher than elsewhere and significant water content differences exist over the sample. Water content tends to homogenise progressively in time, although it is not yet completely homogeneous when t=3000 min.

Test sequences have been simulated with a commercial Finite Element Method code (Comsol) by introducing the mass balance equations for water and air phase,

$$\frac{\partial\left(\phi S_r \rho_w\right)}{\partial t} + \nabla \cdot \left(\rho_w \mathbf{q}_w\right) = 0$$
$$\frac{\partial\left(\phi\left(1-S_r\right)\rho_a\right)}{\partial t} + \nabla \cdot \left(\rho_a \mathbf{q}_a\right) = 0 \quad ; \quad (2)$$

where ρ_i and u_i are density and pressure of the i-th phase, $\mathbf{q}_i$ is specific discharge and ϕ is porosity. Generalised Darcy laws were used to model the flow of both water and air:

$$\mathbf{q}_w = -k_w(S_r)\nabla\left(z + \frac{u_w}{\rho_w g}\right)$$
$$\mathbf{q}_a = -k_w(S_r)\nabla\left(z + \frac{u_a}{\rho_a g}\right) \quad (3)$$

air and water conductivities were then related to the degree of saturation [Bro64, Cor54]:

$$k_w = k_w^{sat} S_r^{\beta}$$
$$k_a = k_a^{dry}(1-S_r^2)(1-S_r)^2 \quad (4)$$

where k_w^{sat} is water conductivity in saturated conditions and k_a^{dry} is air conductivity in dry conditions. The water retention curve was modelled with the relationship [van80]:

$$S_e = \frac{S_r - S_r^{RES}}{1 - S_r^{RES}} = \left(\frac{1}{1+(\alpha s)^n}\right)^{(1-1/n)} \quad (5)$$

where α and n are experimental parameters and $s=u_a-u_w$ is the matric suction.

Decoupled inversion was run to find the values of β (Equation 4) and of the α and n (Equation 5) that minimise the scatter between ERT reconstructions and hydro-mechanical simulations. Figure 24 shows the water retention curves drawn on basis of the inversions, compared with reference experimental points obtained on analogous samples tested in a controlled suction oedometer with axis translation technique (wetting branch).

The agreement with the reference is very good, considering that water retention curve based on the inversions are obtained through back-analysis of a flow process,

and then are ‘dynamic’ water retention curves (since the water content correspondent to a given suction reflects a dynamic condition).

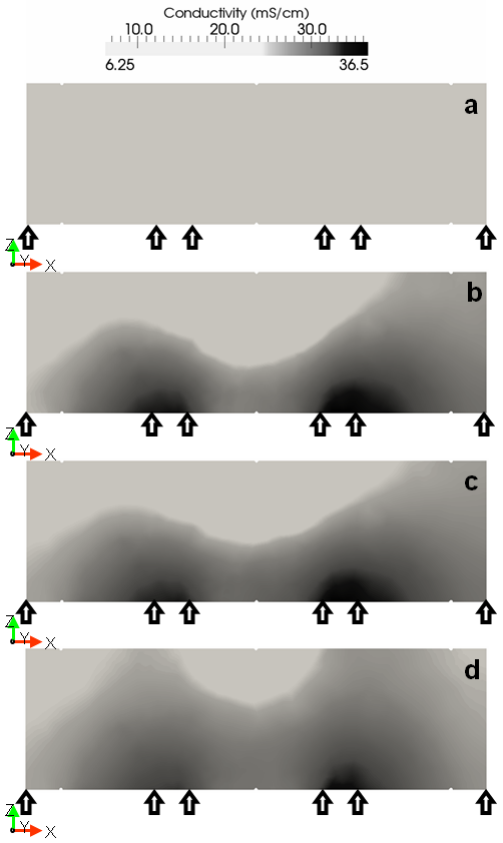

Figure 23: Fast wetting test on a sand sample [Cos12]: time evolution of electrical conductivity over a longitudinal cross-section: a) t=0, b) t=10 min, c) t=110 min, d) t=3000 min (arrows indicate drain positions).

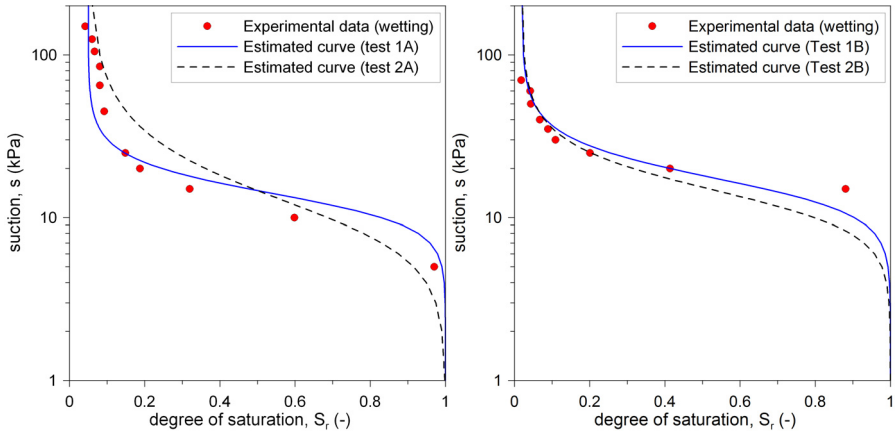

Figure 24: Water retention curves obtained through decoupled inversion of wetting events monitored by means of 3D ERT: (test A) sand sample; (test B) silt sample. 'Experimental data' have been obtained through axis translation technique in a suction controlled oedometer.

6 Acknowledgements

The first author acknowledges the financial support provided by EIG-EURIDICE / SCK.CEN and ONDRAF/NIRAS (Belgium) through a PhD collaboration project for section 3.2, and by NAGRA (Switzerland) through different research projects with CIMNE (Spain) for section 4. The contributions of Dr Marco Caruso (section 2) Prof Antonio Lloret (section 3.1), Dr Analice Lima (section 3.2), Dr Renato Cosentini and Dr Gabriele Della Vecchia (section 5) and Dr Juliana Knobelsdorf are greatly acknowledged.

7 References

[Arn08] Arnedo D., Alonso E.E., Olivella S. and Romero, E. Gas injection tests on sand/bentonite mixtures in the laboratory. Experimental results and numerical modelling. *Physics and Chemistry of the Earth 33, S237-S247*, 2008.

[Ava12] Avanzi F., Caruso M. and Jommi, C. Calibration in the laboratory of capacitance sensors. Submitted for publication to 1st *Pan-American Conf. on Unsaturated Soils 2013, Cartagena, Colombia,* 1-8, 2012.

[Bin96] Binley A., Henry-Poulter S. and Shaw B. Examination of solute transport in an undisturbed soil column using electrical resistance tomography. *Water Resources Research, 32(4), 763-769*, 1996.

[Bin02] Binley, A., Cassiani, G., Middleton, R. and Winship, P. Vadose zone flow model parameterisation using cross-borehole radar and resistivity imaging. *Journal of Hydrology, 267, 147–159*, 2002.

[Bre12] Breen S.J., Carrigan C.R., LaBreque D.J. and Detwiler, R.L. Bench-scale experiments to evaluate electrical resistivity tomography as a monitoring tool for geologic CO2 sequestration. *Int. Jour. Of Greenhouse Gas Control 9, 484 – 494*, 2012.

[Bro64] Brooks, R.H. and Corey, A.J. Hydraulic properties of porous media. *Hydrol., Paper 3*, Colorado State University, Fort Collins, CO, 1964.

[Car11a] Caruso, M. and Jommi, C. A prototype soil column to calibrate numerical models accounting for soil–atmosphere interaction. *In: Unsaturated Soils* E. Alonso & A. Gens (eds.). Taylor & Francis Group, London, UK, Vol. 2, 1121-1132, 2011.

[Car11b] Caruso, M. and Jommi, C. Infiltration and evaporation from bare soil: a comparison between experimental data and predictive models. *In: Unsaturated Soils: Theory and Practice.* A. Jotisankasa, a. Sawangsuriya, S. Soralump & W. Mairaing (eds.). Kasetsart University, Thailand, Vol. II, 791-796, 2011.

[Com08] Comina, C., Foti, S., Musso, G. and Romero, E. EIT oedometer – an advanced cell to monitor spatial and time variability in soil. *Geotechnical Testing Journal ASTM, 31(5), 404-412*, 2008. DOI: 10.1520/GTJ101367

[Com10] Comina, C., Cosentini, R.M., Foti, S. and Musso, G. Electrical Tomography as laboratory monitoring tool. *Rivista Italiana di Geotecnica, 1, 9-20*, 2010.

[Com11] Comina C., Cosentini, R.M., Della Vecchia, G., Foti, S. and Musso G. 3D-electrical resistivity tomography monitoring of salt transport in homogeneous and layered soil samples. *Acta Geotechnica, 6 (4), 195-203*, 2011.

[Cor54] Corey, A.T. The interrelations between gas and oil relative permeabilities. *Producers Monthly, 19, 38-41*, 1954.

[Cos12] Cosentini, R.M., Della Vecchia, G., Foti, S. and Musso, G. Estimation of the hydraulic parameters of unsaturated samples by electrical resistivity tomography. *Géotechnique, 62(7), 583-594*, 2012. DOI:10.1680/geot.10.P.0662012

[Dam09] Damasceno, V.M., Fratta, D. and Bosscher, P.J. Development and validation of a low-cost electrical tomographer for soil process monitoring. *Canadian Geotechnical Journal, 4, 842-854*, 2009.

[Fin07] Finsterle, S. ITOUGH2 User's Guide, Report LBNL-40040, Lawrence Berkeley National Laboratory, Berkeley, CA, USA, 2007.

[Har03] Harrington, J.F. and Horseman, S.T. Gas migration in KBS-3 buffer bentonite. Sensitivity of test parameters to experimental boundary conditions. SKB Technical Report TR-03-02, Stockholm, Sweden, 2003.

[Hor99] Horseman, S.T., Harrington, J.F. and Sellin, P. Gas migration in clay barriers. *Engineering Geology 54, 139-149*, 1999.

[Koe08] Koestel, J., Kemna, A., Javaux, M., Binley, A. and Vereecken H. Quantitative imaging of solute transport in an unsaturated and undisturbed soil monolith with 3-D ERT and TDR. *Water Resources Research, 44, W12411, 17,* 2008. DOI:10.1029/2007WR006755

[LaB04] LaBreque, D.J., Sharpe, R., Wood, T. and Heath, G. Small scale electrical resistivity tomography of wet fractured rocks. *Ground Water, 42(1), 111-118*, 2004.

[Lim10] Lima, A., Romero, E., Gens, A., Muñoz, J. and Li, X.L. Heating pulse tests under constant volume on Boom clay. *Journal of Rock Mechanics and Geotechnical Engineering, 2(2), 124–128,* 2010.

[Lim11] Lima, A. *Thermo-hydro-mechanical behaviour of two deep Belgian clay formations: Boom and Ypresian clays.* PhD Thesis. Universitat Politècnica de Catalunya, Spain, 2011.

[Llo07] Lloret, A. and Villar, M.V. Advances on the knowledge of the thermo-hydro-mechanical behaviour of heavily compacted ''FEBEX'' bentonite. *Physics and Chemistry of the Earth, 32, 701–715*, 2007.

[Mic03] Michot, D., Benderitter, Y., Dorigny, A., Nicoullaud, B., King, D. and Tabbagh, A. Spatial and temporal monitoring of soil water content with an irrigated corn crop cover using surface electrical resistivity tomography. *Water Resources Research*, *39(5), 1138,* 2003. DOI:10.1029/2002WR001581.

[Mil84] Milly P. C. D.. A simulation analysis of thermal effects on evaporation from soil. *Water Resources Research*, *20(8), 1087-1098,* 1984.

[Muñ09] Muñoz, J.J., Alonso, E.E. and Lloret, A. Thermo-hydraulic characterisation of soft rock by means of heating pulse tests. *Géotechnique, 59 (4), 293-306*, 2009.

[Oli94] Olivella, S., Carrera, J., Gens, A. and Alonso, E.E. Nonisothermal multiphase flow of brine and gas through saline media. *Transport in Porous Media, 15, 271-293*, 1994.

[Oli96] Olivella, S., Gens, A., Carrera, J. and Alonso, E.E. Numerical formulation for a simulator (CODE_BRIGHT) for the coupled analysis of saline media. *Engineering Computations, 13(7), 87-112*, 1996.

[Oli08] Olivella, S. and Alonso, E.E. Gas flow through clay barriers. *Géotechnique 58(3),157–176*, 2008.

[Ols99] Olsen, P.A., Binley, A., Henry-Poultier, S. and Tych W. Characterizing solute transport in undisturbed soil cores using electrical and X-ray tomographic methods. *Hydrol. Process. 13, 211-221*, 1999.

[Phi57] Philip J. R. and de Vries D. A. Moisture movement in porous materials under temperature gradients. *EOS Trans. AGU, 38, 222-232,* 1957.

[Pin02a] Pintado, X. *Caracterización termo-hidro-mecánica de arcillas expansivas*. PhD Thesis, Universitat Politècnica de Catalunya, Spain (in Spanish), 2002. http://www.tdx.cat/bitstream/handle/10803/6227/TESIS.pdf

[Pin02b] Pintado, X., Ledesma, A. and Lloret, A. Backanalysis of thermohydraulic bentonite properties from laboratory tests. *Engineering Geology, 64, 91–115*, 2002.

[Pol12] Pollock, D. and Cirpka, O.A. Fully coupled hydrogeophysical inversion of a laboratory salt tracer experiment monitored by electrical resistivity tomography. *Water Resources Research, 48, W01505, 13,* 2012. DOI:10.1029/2011WR010779.

[Pru99] Pruess, K., Oldenburg, C. and Moridis, G. TOUGH2 User's Guide, Version 2.0, Lawrence Berkeley National Laboratory, LBNL-43134, 1999.

[Rom10] Romero, E., Arnedo, D., Gómez, R., Alonso, E.E. and Marschall, P. Gas injection laboratory experiments on Opalinus clay (preliminary results). Book of abstracts *Clays in Natural and Engineered Barriers for Radioactive Waste Confinement*, Nantes, France, March 29–April 1 2010. 4th International Meeting Andra (France), in cooperation with Nagra (Switzerland), Ondraf/Niras (Belgium) and SKB (Sweden). O/05/4: 113-114, 2010.

[Rom12a] Romero, E., Senger, R. and Marschall, P. Air Injection laboratory experiments on Opalinus clay. Experimental techniques, results and analyses. *Proceedings Shale Workshop EAGE Conferences*, Barcelona, Spain, January 23-25, 2012. C07: 96-100, 2012.

[Rom12b] Romero, E., Senger, R., Marschall, P. and Gómez, R. Air tests on low-permeability claystone formations. Experimental results and simulations. Theme lecture. *Int. Workshop 'AMTSS - Advances in Multiphysical Testing of Soils and Shales'*, EPFL Lausanne (Switzerland), 3 - 5 September, 2012.

[Sin05] Singha, K. and Gorelick, S. M. Saline tracer visualized with three-dimensional electrical resistivity tomography: Field-scale spatial moment analysis. *Water Resources Research, 41, W05023*, *17,* 2005, DOI:10.1029/2004WR003460.

[Sen12] Senger R., Romero E., Ferrari A. and Marschall P. Characterization of gas flow through low-permeability claystone. Laboratory experiments and two-phase flow analyses. Extended abstract submitted to *Clays in Natural and Engineered Barriers for Radioactive Waste Confinement*, *4th International Meeting Andra* (France), Montpellier, France, 22-25 October, 2012.

[van80] van Genuchten, M.Th. A closed-form equation for predicting the hydraulic conductivity of unsaturated soils. *Soil Sci. Soc. Am. J. 44, 892-898*, 1980.